Nickel-Iron Alloy Nanoparticle Characteristics Pre- and Post-Reaction With Orange G

SHELBY L. FOSTER [1], **PRASHANT ACHARYA**[2], **MOJTABA ABOLHASSANI**[2], **SKYLAR WATSON**[3,4],
SHELDON SHINN[5,6], **AND LAUREN F. GREENLEE** [3]

[1]University of Arkansas and CatalyzeH2O, LLC, Elkins, AR 72727 USA
[2]University of Arkansas, Fayetteville, AR 72701 USA
[3]Department of Chemical Engineering, University of Arkansas, Fayetteville, AR 72701 USA
[4]EnviroTech, Modesto, CA 95358 USA
[5]Department of Mechanical Engineering, University of Arkansas, Fayetteville, AR 72701 USA
[6]Walmart, Rogers, AR 72756 USA

CORRESPONDING AUTHOR: LAUREN F. GREENLEE (e-mail: shelby@catalyzeh2o.com)

ABSTRACT Bimetallic nanoparticles comprised of iron and nickel were synthesized, characterized, and evaluated to optimize the ideal metal ratio for azo dye removal from water systems. Results show that changing the molar ratio of nickel to iron caused different removal rates, as well as the extent of overall elimination of azo dye from water. Lower molar ratios, from Ni_1Fe_{10} to $Ni_{2.5}Fe_{10}$, exhibited a higher removal efficiency of 80–99%. Higher concentrations of Ni in the catalyst, from Ni_3Fe_{10} to Ni_5Fe_{10}, resulted in 70–90% removal. The lower molar ratios of Ni exhibited a consistent removal rate of 0.11 g/L/min, while the higher molar ratios of Ni displayed varying removal rates of 0.1–0.05 g/L/min. A second order kinetic model was fit to the first twenty minutes of the reaction for all nickel to iron compositions, where there is a decrease in rate constant with an increase in molar ratio. During the last forty minutes of reaction, azo dye removal fit a zero order kinetic model. All as-synthesized nanoparticle samples were found to be structurally disordered based on the lack of distinct peaks in XRD spectra. Post-reaction samples were found to have Fe_2O_3 and FeOOH cubic peaks.

INDEX TERMS Azo dye, nanoparticles, iron, nickel, Orange G.

I. INTRODUCTION

Dye contamination from industrial chemical waste is a major contributor to wastewater contamination. The textile industry alone produces roughly 10000 tons of synthetic dye, and of that, 65% are characterized as azo dyes [1], [2]. Azo dyes present an ecological and human health risk due to a cleaving process of the N = N double bond, which occurs in liver enzymes and intestinal microflora [3]. After the cleaving process, the resulting aromatic amines such as benzidine, 4-aminobiphenyl, and 2-naphthylamine are highly toxic and carcinogenic [4]. During the textile dyeing process, 10-25% of textile dyes are lost and 2-20% are directly imparted into the local environment as contaminated effluents [5].

Due to the recalcitrance of azo dyes, recent research has explored reactive monometallic and bimetallic nanoparticle treatment [6]–[8]. In general, the development of nanostructured, reactive materials for water treatment applications holds great promise due to the reactive degradation and improved removal processes that have been demonstrated [9]–[11]. In particular, both laboratory-scale and pilot-scale research studies have demonstrated that iron-based nanostructured materials, such as iron nanoparticles, are able to remove a wide variety of water contaminants, including dyes [12], [13], chlorinated organics [14], [15], pharmaceutical compounds [16], [17], and heavy metals [18], [19], through both oxidative and reductive reaction mechanisms. The process for the decomposition of the dyes by iron-based nanoparticles results from electron transfer from the metallic nanoparticle to the dye, which breaks the azo dye N = N double bond, creating a solution composed of aromatic amines [8]. These aromatic

amines are subsequently more biodegradable than the parent azo dye molecule because the lone pair of electrons on the nitrogen atom is conjugated into the benzene ring, thereby losing the ability to engage in hydrogen bonding and making the electrons less stable [20]. Despite the advantages of iron nanoparticles as an inexpensive and highly reactive material, monometallic iron nanoparticles are also limited by slower dye removal rates, fast deactivation due to oxidation, and pH dependence, as compared to bimetallic counterparts [21]. Iron nanoparticle lifetime remains a critical challenge particularly in oxidative environments, where the nanoparticles quickly react with water and oxygen to form non-reactive iron oxide compounds. Thus, there remains a need to investigate approaches to extend the lifetime as well as to enhance the performance of iron-based nanoparticles.

Bimetallic iron-based nanoparticles remain an important approach to extending iron-based nanoparticle lifetime and reactivity. Research has been conducted using precious metals, such as palladium, platinum, silver, and gold, as the second metal, but these choices are not economically feasible for large scale treatment [22], [23]. An alternative approach is to use another non-precious transition metal, such as nickel, as the second metal in a bimetallic iron-based nanoparticle, and research has shown that iron-nickel nanoparticles are a viable catalyst to decolorize and degrade azo dyes [8], [24], [25]. Not only are these NiFe bimetallic nanoparticles cost-effective, but the nanoparticles also exhibit enhanced reactivity compared to monometallic iron nanoparticles [8]. The nanoparticle dosage, pH, and temperature are factors proven in the literature to impact NiFe reactivity in the aqueous environment [7], [8], [26]–[28]. In previous work, we observed the morphology (i.e., core shell vs. alloy) of the bimetallic nanoparticles changes the kinetics of the reaction, indicating different processes controlling the reaction rate [29]. ANiFe nanoparticles promote different degradation pathways dependent on surface characteristics. NiFe nanoparticles have been found to degrade Orange G through hydrogen transfer, but oxidized NiFe nanoparticles promote the generation of hydroxyl radicals leading to an oxidative pathway [8]. NiFe alloy nanoparticles are commonly found to follow pseudo-first-order reaction for azo dye removal, but our synthesized alloy nanoparticles were found to follow pseudo-second-order [7], [8], [27], [29], [30]. The kinetic discrepancies between our work and literature lead to further investigation of surface characteristics of the nanoparticles pre- and post- reaction to explain kinetic trends.

In this study, the azo dye, Orange G, was used as a representative dye contaminant in simulated, synthetic wastewater solutions. Orange G is a common model contaminant and has similar structural characteristics to other azo dyes but is non-carcinogenic and non-mutagenic. Bimetallic NiFe alloy oxide nanoparticles were synthesized via an aqueous solution-based reduction reaction, and the molar ratio of the two metals (nickel/iron) was evaluated. Nanoparticles with molar ratios ranging from Ni_1Fe_{10} to Ni_5Fe_{10}, were chosen due to previous work conducted [29] and were tested in batch

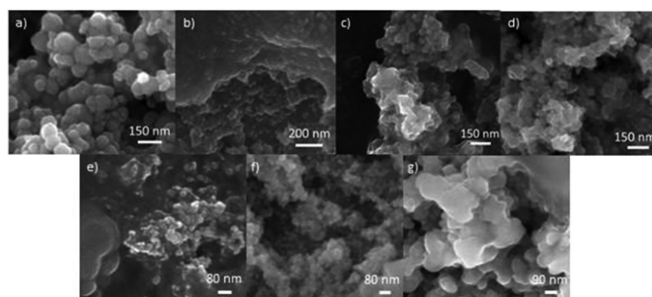**FIGURE 1.** Scanning electron microscopy images of: (a) Fe monometallic, (b) Ni monometallic, (c) Ni_1Fe_{10} composition, (d) Ni_2Fe_{10} composition, (e) Ni_3Fe_{10} composition, (f) Ni_4Fe_{10} composition, and (g) Ni_5Fe_{10} composition nanoparticles used in experiments for treatment of the Orange G dye.

reactors for the removal of Orange G over time. The nanoparticle surface and bulk characteristics were investigated pre- and post-reaction to understand how nanoparticle chemistry changes and to explain differences in removal efficiency. The performance efficiency of the nanoparticles was evaluated quantitatively through concentration changes of Orange G in synthetic water samples; the kinetics of Orange G dye removal are discussed and presented as a function of nanoparticle composition. The nanoparticles were characterized using scanning electron microscopy (SEM), energy dispersive x-ray spectroscopy (EDX), x-ray diffraction (XRD), and x-ray photoelectron spectroscopy (XPS).

II. METHODS AND PROCEDURES
A. MATERIALS
The source of iron for synthesis was ferrous sulfate heptahydrate ($FeSO_4•7H_2O$), while the nickel precursor was nickel (II) chloride hexahydrate ($NiCl_2•6H_2O$). Both metal salts were supplied by Alfa Aesar. The stabilizers used for synthesis were amino tris (methylene phosphonic acid) (ATMP), supplied from Dequest (Italmatch), and poly(N-vinyl-2-pyrrolidone) (PVP) (MW = 40000 g/mol), supplied from Tokyo Chemical Industries (TCI). The reducing agent used was a fine granular sodium borohydride ($NaBH_4$) from EMD Millipore Corporation. All synthesis and synthetic wastewater solutions were made with purified water (Millipore Milli-Q Integral, 18 MΩ).

B. NANOPARTICLE SYNTHESIS
The synthesis method utilized in this experiment was an aqueous batch reduction method (Fig. 1) [31], [32]. The synthesis was performed in 20 mL batches in 250 mL or 500 mL three-neck borosilicate flasks. The first step in the synthesis required dissolving the iron precursor in purified water at 10 g/L and adding in stabilizer. The iron was stabilized with 0.5 mL of 214.5 g/L ATMP stock solution. After the iron precursor and ATMP were added into the three-neck flask, the flask was placed on an orbital shaker for fifteen minutes to mix the solution. Argon was bubbled into the solution during mixing to minimize unwanted oxidation of the iron. After the iron

and ATMP were mixed for fifteen minutes, PVP-stabilized nickel was added to the solution. The final molar ratio desired determined the amount of nickel to be added, and this ratio ranged from 0.1 mol nickel:mol iron to 0.5 mol nickel:mol iron (Ni_1Fe_{10} - Ni_5Fe_{10}). PVP was used for nickel stabilization at a constant ratio of 0.005 mol PVP:mol Ni. The nickel and PVP were added together and mixed into solution, added to the three-neck flask with the stabilized iron, and then bubbled with argon for another fifteen minutes. After this second fifteen-minute mixing period, the reducing agent was added. Sodium borohydride was used to reduce the metal solution at a ratio of 2.6 mol sodium borohydride to total moles of iron and nickel in the solution. The sodium borohydride was added dropwise to the flask at a rate of roughly 10 mL per minute, and then the solution was placed under vacuum and mixed for fifteen minutes. The addition of the sodium borohydride reduces the iron and nickel salts to form bimetallic nanoparticles and a hydrogen gas product, as shown in the formal reaction below.

$$Fe^{2+}\left(Ni^{2+}\right) + 6H_2O + 2BH_4^{-}$$
$$\rightarrow Fe^0\left(Ni^0\right) + 2B(OH)_3 + 7H_2 \quad (1)$$
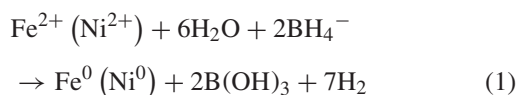
Excess sodium borohydride was used in the synthesis procedure to account for the side reaction between borohydride and water molecules. After the third and final mixing period, the solution of nanoparticles was removed from the three-neck flask, placed in a 50 mL centrifuge tube, and centrifuged at 7800 rpm at 23 °C for two minutes. This step separated the nanoparticles from the solution allowing for easy disposal of the supernatant. The supernatant was removed to discard excess salts and stabilizer. Nanoparticles were then resuspended in methanol, sonicated for fifteen minutes, and bubbled with argon in the centrifuge tube for fifteen minutes to minimize oxidation.

C. ORANGE G TREATMENT
The nanoparticles and Orange G were added at equal volumes of 1 g/L stock solution to a 20 mL total solution volume, and a timer was started immediately after the addition of the two solutions. Once the two solutions were added together, the reactor was placed in a rotator mixer and continuously mixed. This approach allowed the nanoparticles to remain dispersed throughout the dye solution. Samples were then taken from the sample at 2-minute intervals for the first 20 minutes, 5-minute intervals between 20 and 40 minutes, and 10-minute intervals until 60 minutes was reached. Time intervals increased throughout the experiment due to faster reaction rates of the particles with Orange G within the first 20 minutes and a change in rate after roughly 25 minutes. A small sample was removed through a syringe at each time interval, centrifuged, and tested in a UV-Vis spectrophotometer at a wavelength of 530 nm. A standard curve for Orange G was measured for each experiment and used to quantify experimental sample concentrations.

D. CHARACTERIZATION
Nanoparticle morphology was evaluated through scanning electron microscopy (SEM) (FEI Nova 200 NanoLab dual beam SEM microscope), and energy dispersive x-ray spectroscopy (EDX) was used during SEM imaging to determine nanoparticle composition. To prepare samples for SEM imaging, a 10 g/L solution of nanoparticles dispersed in purified water was centrifuged. The supernatant was removed, and methanol was added to the nanoparticles. After the particles were immersed in methanol and resuspended, 150 μL were drawn out, drop-casted onto a 6 mm diameter conductive carbon tab, and placed in a laboratory hood to dry. Images were captured between 5 keV and 15 keV electron beam voltage between 150,000x and 350,000x magnification.

X-ray photoelectron spectroscopy (XPS; PHI Versaprobe 5000 with PHI MultiPack data analysis software) was used to analyze the surface chemical composition of the nanoparticles before and after Orange G treatment. A monochromated Al Kα source was used to perform the experiment. Full survey scans (0 eV–1400 eV) along with detailed scans of iron (700 eV–740 eV), nickel (844 eV–894 eV), carbon (278 eV–298 eV), and oxygen (523 eV–543 eV) were conducted on the nanoparticles.

High resolution x-ray diffraction (XRD, Philips X'Pert-MRD diffractometer, Cu Kα radiation source) was used to determine the crystalline structure of the nanoparticles. The voltage of 45.0 kV and a current of 40.0 mA were applied with the scanning speed of 1 min^{-1}. XRD patterns were taken within the region of 2θ from 25 to 65°. Each sample was dispersed in methanol and then drop casted on a glass slide drop by drop for about 30 minutes. The samples were kept in a chemical hood for about 1 hour to dry.

III. RESULTS
A. AS-SYNTHESIZED NANOPARTICLE CHARACTERIZATION: MORPHOLOGY AND COMPOSITION
SEM images of the nanoparticles used in Orange G experiments are shown in Fig. 1. Generally, the nanoparticles are roughly spherical in morphology and are visibly covered in organic ligand stabilizer. ATMP is used for iron precursor stabilization, while PVP is used for nickel precursor stabilization. ATMP is a low molecular weight chelator, while PVP is a polymer, and the difference in the size of the molecules is evident in the physical thickness of the organic layer surrounding the nanoparticles in Fig. 1(a) and 1(b), for iron nanoparticles and nickel nanoparticles, respectively. This organic layer remains even if the nanoparticles are rinsed multiple times. Iron-only and nickel-only nanoparticles appear to have a more spherical morphology than the bimetallic nanoparticles, which appear to have a rougher, inhomogeneous shape. The nickel nanoparticles are visibly smaller than the iron nanoparticles, and the bimetallic nanoparticles vary in size and size dispersity. All of the nanoparticle samples appear to agglomerate together, which is likely due to the effect of the ATMP and PVP stabilizers, as well as the effect of drying colloidal,

TABLE 1. Energy Dispersive X-Ray Spectroscopy Data for Ratios of Nickel to Iron

Theoretical Ratio	FE AT. %	Ni at. %
Ni_1Fe_{10}	90.9	9.1
Ni_2Fe_{10}	81.8	18.2
Ni_3Fe_{10}	76.7	23.3
Ni_4Fe_{10}	71.1	28.9
Ni_5Fe_{10}	66.4	33.6

FIGURE 2. XRD spectra of (a) Ni_1Fe_{10}, (b) $Ni_{1.5}Fe_{10}$, (c) Ni_2Fe_{10}, (d) $Ni_{2.5}Fe_{10}$, (e) Ni_3Fe_{10}, (f) $Ni_{3.5}Fe_{10}$, (g) Ni_4Fe_{10}, and (h) Ni_5Fe_{10} as-synthesized (black) and post-reaction (red) nanoparticles. Peaks for Ni_5Fe_{10} were identified as (i) for the as-synthesized sample and (ii) and (iii) for the post-reaction sample. Peak (i) is found at 44.2° and is only seen for Ni_5Fe_{10}. Peak (ii) and (iii) are found to correlate with Fe_2O_3 and FeOOH crystalline peaks assumed to occur through oxidation during the reaction.

hydrophilic nanoparticles onto an SEM stub. In the bimetallic samples, especially at higher nickel ratios, individual nanoparticles are more difficult to distinguish, which suggests possible particle aggregation, distorted spherical morphology, and the impact of higher PVP content. Nanoparticle size was quantified from SEM images with ImageJ software. Particle diameters with calculated standard deviation are shown in Fig. S1 of the Supplemental Information.

EDX measurements were obtained during SEM imaging to quantify and verify the molar ratio of Ni to Fe in the nanoparticles. EDX is a semi-quantitative measurement technique due to the lack of standards used to directly compare with experimental samples. EDX is typically expected to have an error of up to 5–10% and is not an appropriate technique for analysis of low z elements such as oxygen and nitrogen. Results, shown in Table 1, demonstrate that measured compositions for Fe and Ni in the synthesized nanoparticles align well with the theoretical ratios of Ni to Fe calculated for metal precursor addition to the synthesis solutions. These EDX results thus confirm that the as-synthesized nanoparticles used in Orange G removal studies contained the target compositions.

B. CHARACTERIZATION OF NANOPARTICLES PRE- AND POST-AQUEOUS ORANGE G REMOVAL

XPS and XRD data were obtained for as-synthesized nanoparticles and nanoparticles post Orange G removal from aqueous batch solutions. We expected that our nanoparticles start as-synthesized as a mix of metallic and oxide species, based on prior work [33], [34]. For this study, we were particularly interested in understanding how the oxidation state, bulk structure, and surface chemistry of the nanoparticles changed as a function of azo dye removal from water and as a function of as-synthesized properties. First, we focus on an analysis of the bulk crystallinity of the nanoparticles. Apart from the Ni_5Fe_{10} as-synthesized nanoparticle sample, all as-synthesized nanoparticles resulted in spectra with no visible peaks; for the Ni_5Fe_{10} as-synthesized nanoparticles, a small, broad peak is visible at 44.2° (Fig. 2(h), black spectrum). This result suggests that all of the as-synthesized nanoparticles were comprised of a highly disordered bulk structure, consistent with prior results based on the aqueous ATMP Fe nanoparticle synthesis approach [35], [36]. The XRD spectra of each nanoparticle sample post-reaction are shown in
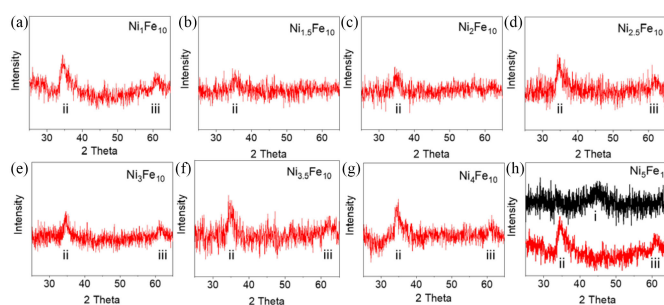
Fig. 2(a)–(g) in red, where spectra for as-synthesized nanoparticles were excluded in Fig. 2a-(g) due to the lack of peaks.

The XRD spectra of Ni_5Fe_{10} nanoparticle samples for both as-synthesized and post-reaction conditions are shown in Fig. 2(h) with each peak labeled as i, ii, or iii. Peaks ii and iii are also labeled in Fig. 2(a)–(g). In Fig. 2(h), the broad peak at 44.2° (peak i) is identified as the primary peak for metallic Ni and Fe species in a NiFe (111) bulk alloy face centered cubic (fcc) crystalline structure [37]–[40]. Due to the high Fe content in the as-synthesized samples, we do not see the two peaks that would typically be expected to appear at 52° and 76.5° and which correlate to (200) fcc and (220) fcc; these two additional peaks are often only seen in the bulk diffraction lattice patterns for NiFe alloy materials with high Ni content (i.e., Ni at. % ≥ 67%) [37]–[39]. NiFe alloy nanoparticles for treating azo dye literature indicate that NiFe alloy nanoparticle structure varies for studies due to differing synthesis procedures [7], [27], [41]. There is a lack of post experimental XRD analysis to determine phase shifts in the literature. The post-reaction Ni_5Fe_{10} nanoparticle sample shows the disappearance of peak (i) and the appearance of two new peaks (ii and iii). The two new peaks are identified as (ii) the Fe_2O_3 (104) rhombohedral crystalline facet and (iii) the FeOOH (221) crystalline facet [42], [43]. FeOOH (221) structure has not been seen in previous NiFe alloy nanoparticle literature for treating an azo dye compound.

The remaining XRD results for the other tested nanoparticle ratios post-reaction are shown in Fig. 2, indicating a similar, general trend of the formation of the two oxide/hydroxide (ii and iii) Fe_2O_3 and FeOOH crystalline peaks through oxidation occurring during the reaction. All the nanoparticle ratios exhibit the two new peaks post-reaction except the $Ni_{1.5}Fe_{10}$ and Ni_2Fe_{10} compositions. Instead, $Ni_{1.5}Fe_{10}$ and Ni_2Fe_{10} only present a low intensity peak (ii). Generally, the lack of well-defined diffraction peaks in post-reaction samples suggests that all of the as-synthesized and post-reaction nanoparticle materials are disordered structurally. The Orange G dye removal process thus results in slight structural changes
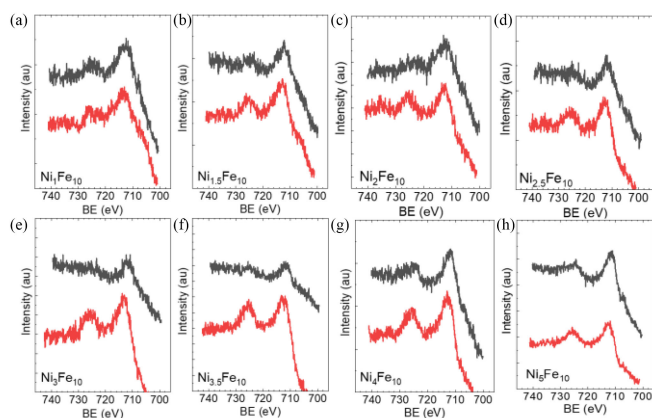
FIGURE 3. Detailed Fe scans of (a) Ni_1Fe_{10}, (b) $Ni_{1.5}Fe_{10}$, (c) Ni_2Fe_{10}, (d) $Ni_{2.5}Fe_{10}$, (e) Ni_3Fe_{10}, (f) $Ni_{3.5}Fe_{10}$, (g) Ni_4Fe_{10}, and (h) Ni_5Fe_{10} as-synthesized (black) and post-reaction (red) nanoparticles. BE = binding energy.

FIGURE 4. Detailed Ni scans of (a) Ni_1Fe_{10}, (b) $Ni_{1.5}Fe_{10}$, (c) Ni_2Fe_{10}, (d) $Ni_{2.5}Fe_{10}$, (e) Ni_3Fe_{10}, (f) $Ni_{3.5}Fe_{10}$, (g) Ni_4Fe_{10}, and (h) Ni_5Fe_{10} as-synthesized (black) and post-reaction (red) nanoparticles.

from highly disordered (lack of distinctive peaks) to a slightly more crystalline oxide-hydroxide structures after bulk oxidation as a result of the reaction; the chemical phase and oxidation state changes are more significant than changes to bulk crystallinity.

The XPS results for the as-synthesized and post-reaction samples are shown in Fig. 3 for the Fe 2p binding energy region. The $Fe2p^{3/2}$ peak is observed in each of the as-synthesized samples (black line) and occurs at the peak position of 711.3 to 711.8 eV range. This peak position indicates either an alpha or gamma hydroxide species [44]–[47]. The $Fe2p^{1/2}$ peak at 724 eV is present for Ni_4Fe_{10} and Ni_5Fe_{10} as-synthesized samples, indicating the presence of iron oxide and iron hydroxide species [44], [48]. The $Fe2p^{3/2}$ and $Fe2p^{1/2}$ peaks are similar for NiFe alloy nanoparticles found in literature for the treatment of azo dyes [8], [41]. The $Fe2p^{1/2}$ peaks are harder to identify from the background noise for the Ni_1Fe_{10}-$Ni_{3.5}Fe_{10}$ molar ratios for the as-synthesized samples which indicates that the samples had less Fe at the surface of the particles. Fig. 3(g) and 3(h) show a small shoulder at 707 eV, which is indicative of Fe metal [44], [49]. As Ni content decreases from $Ni_{3.5}$ to Ni_1, the Fe metal shoulder is no longer present. This result indicates that as less Ni is used in the synthesis of the nanoparticles, less Fe metal is present on the surface of the nanoparticles. This conclusion could be explained as the additional Ni content in Ni_4Fe_{10} and Ni_5Fe_{10} is thought to help to slow the oxidation of Fe in the nanoparticles, allowing a greater amount of Fe^0 and a Fe metal shoulder to be present for the as-synthesized samples [8].

Once the nanoparticles are used in the reaction to remove azo dye, the Fe metal shoulder is no longer present in either Fig. 3(g) and 3(h) post-reaction red spectra. Bokare et al. observed a shift in Fe metal to a lower binding energy that indicated the establishment of NiFe electrochemical cell to slow oxidation in the post reaction nanoparticles [8]. Therefore, the disappearance of the peak for the post reaction in this study
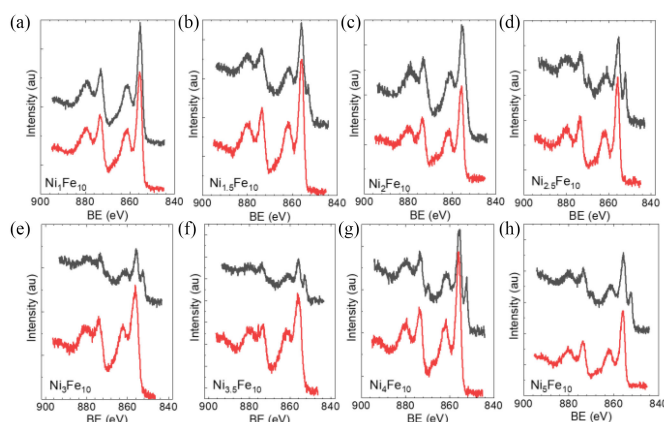
indicates a lack of electrochemical cell establishment, which led to faster oxidation. In addition, the $Fe2p^{3/2}$ peak shifts slightly to higher binding energy (eV) in the post-reaction sample for all ratios, as compared to the as-synthesized sample, indicating a subtle shift in the chemistry from hydroxide to oxide species. The Fe2p peaks increase in peak intensity from the as-synthesized sample to the post-reaction sample, which indicates a relative increase in the amount of Fe found at the nanoparticle surface. This result is supported by the diffusive oxidation process of Fe, where Fe^0 species will migrate outward and oxidize at the particle surface [50]. The peak positions for the iron spectra for all eight as-synthesized samples are the same, which suggests that regardless of as-synthesized composition, all of the samples contain similar initial iron surface chemistry, with iron species largely in the Fe^{3+} oxidation state. Once the reaction with Orange G occurs, the peaks increase in intensity from the background noise and peak locations shift to higher BE for all eight samples. Again, these results indicate that despite changes in iron-nickel atomic composition in the bimetallic nanoparticles, the surface chemistry changes that occur to iron as a result of reaction with Orange G are similar.

Fig. 4 shows detailed scans of the Ni 2p binding energy region of each of the ratios before and after reaction with Orange G. Each ratio has four distinct peaks at 855.4 eV, 861.3 eV, 873.1 eV, and 879.6 eV for the as-synthesized samples. The $Ni2p^{3/2}$ peak at 855.4 eV indicates the presence of nickel hydroxide, and the $Ni2p^{1/2}$ peak at 873.1 eV indicates the presence of nickel oxide [44], [51]. The $Ni2p^{3/2}$ and $Ni2p^{1/2}$ peaks are similar for NiFe alloy nanoparticles found in literature for the treatment of azo dyes [8]. The peaks at 861.3 eV and 879.6 eV are satellite peaks which indicate an electron correlation in the system [8], [52]. The larger concentrations of Ni starting at $Ni_{2.5}Fe_{10}$ ratio show an additional peak at 852.2 eV, which indicates the presence of Ni metal in the nanoparticles [53]. Ni metal was present for NiFe alloy nanoparticles in the literature for the treatment of azo dyes [8], [41]. Similar to the Fe metal peaks, the Ni metal
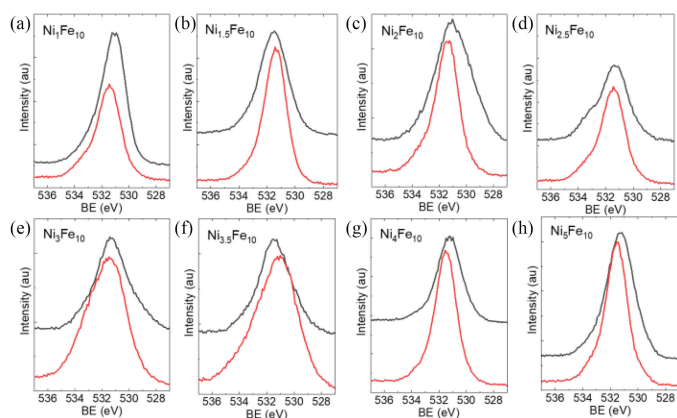
FIGURE 5. Detailed oxygen scans of (a) Ni_1Fe_{10}, (b) $Ni_{1.5}Fe_{10}$, (c) Ni_2Fe_{10}, (d) $Ni_{2.5}Fe_{10}$, (e) Ni_3Fe_{10}, (f) $Ni_{3.5}Fe_{10}$, (g) Ni_4Fe_{10}, and (h) Ni_5Fe_{10} as-synthesized (black) and post-reaction (red) nanoparticles.

FIGURE 6. The decolorization of Orange G over time with nickel nanoparticles, iron nanoparticles, and bimetallic nanoparticles at specific molar ratios of nickel to iron (Ni1Fe10, Ni_2Fe_{10}, Ni_3Fe_{10}, Ni_4Fe_{10}, and Ni_5Fe_{10}), compared to an Orange G control.

peak disappears in the post-reaction spectra, indicating that the Ni metal oxidizes during the reaction. The peak positions for nickel spectra for all eight as-synthesized samples are the same, which suggests that, regardless of composition, the samples are all in the Ni^{2+} oxidation state [53]. Once the reaction occurs, the peaks increase in intensity, indicating an increase in Ni atoms in the Ni^{2+} oxidation state on the surface, likely due to oxidation [54].

Detailed scans of the oxygen 2p binding energy region (Fig. 5) show a broad peak for all the as-synthesized and post-reaction nanoparticles, which indicates metal oxides and metal hydroxides [51], [55]–[58]. The broad peak can be attributed to both Fe and Ni atoms since oxide and hydroxide peaks were present for both Fe and Ni detailed XPS scans. From as-synthesized to post-reaction nanoparticles, the peak intensity increases, indicating an increase of oxygen on the nanoparticle surfaces post-reaction. For all the ratios except Ni_3Fe_{10} and $Ni_{3.5}Fe_{10}$, the oxygen peak sharpens post-reaction which could be attributed to an increase in metal hydroxides and decrease of metal oxides.

C. ORANGE G REMOVAL FROM SYNTHETIC WATER

Orange G removal from synthetic water was first tested for the monometallic nanoparticles, which serve as control materials for the experimental bimetallic nanoparticle sample set. Results, shown in Fig. S2, demonstrate that nickel nanoparticles alone have no removal efficiency for Orange G. In general, in this study, we measured the loss of Orange G via UV-visible spectrophotometry, and this measurement can reflect both adsorptive removal of Orange G and destructive degradation of Orange G by the nanoparticles. Spectrophotometric measurements do not distinguish between adsorption and degradation, and thus both mechanisms of Orange G removal may occur [8]. However, with the nickel-only nanoparticles, neither mechanism occurs, and no removal of Orange G is observed. In comparison, the iron-only nanoparticles result in removal of Orange G from solution. The iron nanoparticles cause a fast decrease in Orange G concentration within 2 min, from
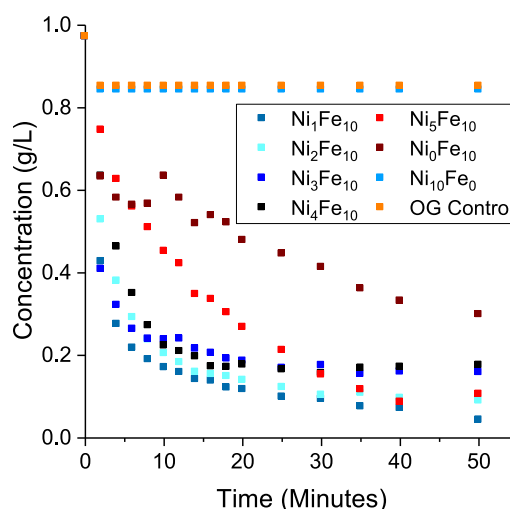
1 g/L to 0.6 g/L. Following this fast removal, the nanoparticles then cause a slow removal of Orange G over the rest of the tested time period up to 60 min. Overall, the iron nanoparticles show a decolorization removal of about 70-80% with a fairly linear decrease in Orange G concentration versus time after 2 min. The control experiment with Orange G tested in solution and no nanoparticles demonstrates that the iron nanoparticles are directly responsible for the removal of Orange G from aqueous solution, and there is no evidence of other removal mechanisms, such as adsorption to the container walls. Although an Orange G treatment efficiency of 70–80% by the iron nanoparticles is substantial, a material with increased removal kinetics, increased lifetime, and increased removal of the dye is desired.

The impact of adding nickel to the iron nanoparticles is demonstrated in the results of Fig. 6, where even the lowest amount of nickel, in the Ni_1Fe_{10} composition, results in a significant increase in the removal rate of Orange G, as well as in the total amount of Orange G removed from the solution. All results shown in the following figures are representative data sets from experiments that were repeated five times. Additional graphs with error bars are reported in the Supplemental Information file. While the error of some of the experiments is significant, suggesting experimental variability, we note that each data set as a function of nickel to iron ratio resulted in the same overall trend. As a result, a single data set is reported in our figures to illustrate the trends and not necessarily to report exact or average data points. Experimental variability is thought to result from the speed of sampling required, particularly during the first 20 min of each experiment, as well as individual human error and variability. Sampling every 2 min was desirable to capture the fast decline in Orange G concentration but resulted in an increase in standard deviation from the overall average.

An increase in the Ni content from Ni_1Fe_{10} to Ni_5Fe_{10} causes a decrease in the removal rate of Orange G, while the overall amount of Orange G removed from solution over 60 min is essentially the same for all Ni to Fe ratios tested. Within the range of Ni to Fe ratios, the removal of Orange G in the first 10 min decreases as the ratio increases from Ni_1Fe_{10} to Ni_3Fe_{10}. At higher ratios, the Ni_4Fe_{10} composition performs better than Ni_3Fe_{10}, and Orange G removal decreases as the ratio increases from Ni_4Fe_{10} to Ni_5Fe_{10}. While the trend in Orange G removal is clearly a function of nanoparticle composition, the variability in nanoparticle size (Fig. S1) may also be influencing the trend in Orange G removal. In particular, when both possible mechanisms of Orange G removal are considered, the available surface area of the nanoparticles would play an important role in both adsorptive removal of Orange G onto the surface of the nanoparticles and the reactive removal of Orange G through reactions with the metals in the nanoparticles [8]. The smaller observed nanoparticle size of the Ni_3Fe_{10} and Ni_4Fe_{10} compositions likely contributes to the increased Orange G removal, as compared to the higher ratio and the larger nanoparticles of the Ni_5Fe_{10} composition. The Ni_4Fe_{10} composition results in a similar Orange G removal rate as the Ni_2Fe_{10} composition, which may also reflect the impact of the smaller measured nanoparticle diameter, even though the ratio of Ni to Fe in the nanoparticles is higher.

To investigate the role of the ratio of Ni to Fe in more detail, additional ratios were tested within the initial range of Ni to Fe. Results, shown in Fig. 7, show a detailed comparison of ratios from Ni_1Fe_{10} to $Ni_{2.5}Fe_{10}$ and Ni_3Fe_{10} to Ni_5Fe_{10}. Within the lower molar ratio range, Orange G removal efficiencies range between 80–99% after 50 minutes of treatment, and within the higher molar ratio range, Orange G removal efficiencies range between 70–90% after 50 minutes of treatment. Nanoparticles with lower amounts of nickel exhibited more consistent trends in treatment of the Orange G, as compared to nanoparticles with higher amounts of nickel. Fig. 7 includes representative data sets of each of the catalysts and their results over a 50 minute treatment period. Further, the larger ratio range resulted in a more variable calculated slope of decline in the initial decrease in Orange G removal. The initial rate of removal over the first 6 min was about 0.11 g/L/min for the lower ratio range (Ni_1Fe_{10} to $Ni_{2.5}Fe_{10}$) versus the higher ratio range (Ni_3Fe_{10} to Ni_5Fe_{10}), which varied from 0.1 g/L/min to 0.05 g/L/min. The differences in treatment performance with the varying molar ratios can be due to a number of reasons, depending on how the dye is being decolorized. In a bimetallic composition, Fe and Ni interact and react through a series of complex electron transfer redox reactions, where both the Fe and the Ni contribute to dye removal. The details of these reactions have been previously reported [8] and are not discussed in detail here.

In the results reported herein, all nanoparticle samples were synthesized on a basis of 1 g/L Fe, where the nickel precursor concentration was changed to obtain the desired Ni to Fe ratio. Thus, our results demonstrate the impact of increasing nickel mass content on an equivalent Fe mass basis. We can draw
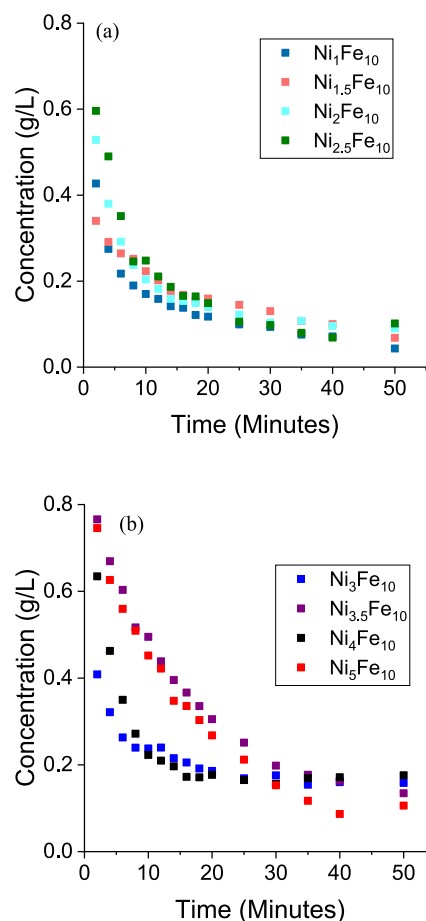

FIGURE 7. Decolorization of Orange G versus time for (a) lower ratios (Ni_1Fe_{10} - $Ni_{2.5}Fe_{10}$) and (b) higher ratios (Ni_3Fe_{10} - Ni_5Fe_{10}) of Ni to Fe.

conclusions about how the increasing nickel mass added to the nanoparticles affects the overall reactivity of the bimetallic nanoparticle. First, the addition of any amount of Ni to a Fe nanoparticle effectively enhances the reactivity of the Fe redox system by adding in additional reactants to the reaction system. This effect of Ni on Fe is observed in all of our experimental results. Electron donation between Fe and Ni is also known to extend the lifetime of the reactivity [8], as can be observed in comparing the iron-only nanoparticles and any bimetallic composition in our data. If we first assume reactive decomposition of the dye is a removal mechanism of the Fe-Ni reaction system, the lower molar ratios can both extend effective Fe nanoparticle lifetime and enhance reactivity, while not blocking the electron transfer sites or adsorption sites at the nanoparticle surface. However, as the nickel content increases, we would expect that there is more nickel at the surface of the nanoparticles, and the adsorption and reaction sites of the surface are no longer optimal for Orange G removal. It is possible that the addition of nickel above a certain amount decreases the availability of electrons available through Fe-Ni redox reactions due to the changing molar ratio of the two metals. Thus, the lower molar ratios, while being more stable than the iron only nanoparticles but perhaps less stable than

the higher molar ratios, are also more efficient at removing Orange G than the higher molar ratios.

Assuming adsorption onto the surface of the nanoparticles is also an important removal mechanism for Orange G, the higher amounts of nickel can simply be blocking or changing optimal adsorption sites for Orange G, resulting in less efficient removal of Orange G from the aqueous solution. Both reactive degradation and adsorption are expected to occur during Orange G removal and are likely interconnected in terms of the overall removal mechanism (i.e., Orange G degradation largely occurs at the surface of the nanoparticles during or after Orange G adsorption). Additional factors that could contribute to variation in Orange G removal efficiency include differences in nanoparticle size [59] and the impact of the stabilizer ligands [60], which are parameters that were not specifically studied in this work. While these parameters may also impact Orange G removal, it is clear that the molar ratio of Ni to Fe in the nanoparticles is an important parameter to control and understand when evaluating the removal efficiency of a target contaminant such as Orange G.

D. KINETIC ANALYSIS

A kinetic rate model analysis of Orange G removal data was performed, and the kinetic rate constants are reported as a function of Ni to Fe molar ratio in Fig. 8. The data were analyzed with zeroth, first, and second order reaction rate equations (outlined in Table S1 the SI) to find the best linear fit.The data did not fit well to a single rate equation for the entire 60 min experiment, suggesting that there are two regions of Orange G decolorization and removal for all nanoparticle samples tested. The data was split into two regions: the first twenty minutes and the last forty minutes. The two regions were investigated separately to determine the accurate reaction rate law. All of the data showed an initial Orange G removal rate with second order rate constants over the first 20 min. of the data showed an initial Orange G removal rate with second order rate constants over the first 20 min. All of the nanoparticles, excluding $Ni_{2.5}Fe_{10}$, Ni_4Fe_{10}, and Ni_5Fe_{10}, shift to a zeroth order reaction rate order from 20 min to 60 min. The last forty minutes for $Ni_{2.5}Fe_{10}$, Ni_4Fe_{10}, and Ni_5Fe_{10} data were unable to adequately fit to a zero, first or second order reaction rate due to variability in points. Second order rate constants are shown in Fig. 8(a) and span the first twenty minutes of the treatment process. An assumption of pseudo-first order is not a valid assumption in our experiments as both reactants, Orange G dye and iron/nickel concentration, decline over time as the dye is removed and the metal constituents are oxidized. Generally, although there is variability in the rate constants, the second order rate constant decreases as the molar ratio of Ni to Fe increases. This result is consistent with the visual observations taken from Figs. 6 and 7, where the lower molar ratios cause a faster decrease in Orange G concentration over the first 20 min of the experiment. However, after 20 min, the reaction rate constant increases with increasing molar ratio of Ni to Fe, as shown in Fig. 8(b). This result is difficult to visually observe in the graphs above but
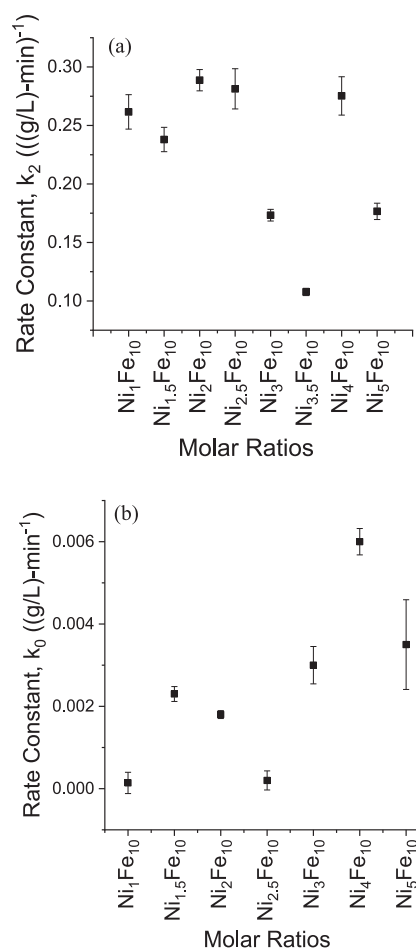
FIGURE 8. a) Second-order kinetic rate constants versus Ni to Fe molar ratios for 20 minutes and b) zero-order kinetic rate constants versus Ni to Fe molar ratios 20 min to 60 min.

suggests that the nanoparticles have an increased lifetime of reactivity over time as the molar ratio of Ni to Fe increases. This result is consistent with the expectation that the addition of Ni to an Fe nanoparticle increases the overall stability of the nanoparticle and thus increases the nanoparticle lifetime in a reactive aqueous system [9]. The shift to a zeroth order reaction rate suggests that after 20 min, the Orange G and metal reactant concentrations no longer influence the removal of Orange G. This shift in reaction rate dependence may signal a shift in overall removal mechanism, where the additional removal of Orange G after 20 min occurs as adsorption sites become available, as adsorbed Orange G is degraded into by-products, and/or as Orange G molecules are adsorbed onto newly-formed oxide/hydroxide surfaces.

The detailed Fe scans (Fig. 3) show that the highest Ni to Fe molar ratios (Ni_4, Ni_5) have Fe and Ni metal present, which indicates that the Ni incorporation helps to preserve the reactive Fe longer than subsequent smaller molar ratios. While the metal reactant concentration no longer controls the reaction rate after 20 min, the greater starting Fe and Ni metal content could possibly influence the increase in reaction rate

constant after 20 minutes through more available Fe later in the testing time. Further, the increased Ni content likely causes the slower reaction kinetics between 0 and 20 min, where the Ni metal at the surface slows Fe oxidation. The trade-off of the increased stability later in the reaction is the decrease in initial reactivity, resulting in a lower initial decline in Orange G concentration. Overall, a greater concentration of Orange G is removed for the nanoparticles with lower molar ratios of Ni to Fe, and the faster removal rate of the lower molar ratios at short timeframes appears to be more significant in the overall removal efficiency of the treatment process, rather than the higher removal rate of the higher molar ratios of Ni to Fe at later timeframes. The trade-off between lifetime and reactivity, as well as overall removal efficiency, must be considered when optimizing a reactive Fe-based material for water treatment applications.

IV. CONCLUSION

Bimetallic alloy nanoparticles were synthesized via an aqueous-phase solution chemical reduction and precipitation method. Specific stabilizers are used to control nanoparticle formation during synthesis, and the ratio of iron and nickel precursors was varied by varying the nickel precursor concentration for a constant iron concentration. The composition of the NiFe bimetallic nanoparticles was confirmed through EDX characterization, and nanoparticle morphology and size were evaluated by SEM. As-synthesized nanoparticles are structurally disordered, but after treatment of Orange G have Fe_2O_3 and FeOOH cubic peaks in the XRD spectra. Zero valent metallic contributions to the as-synthesized nanoparticles are seen for higher NiFe molar ratios but are not present post-reaction, which indicates oxidation occurred. The as-synthesized and post-reaction samples consist of Fe^{3+} and Ni^{2+} in hydroxide and oxide form. For all molar ratios, post-reaction samples resulted in sharper, more intense peaks for both Fe and Ni spectra, which suggests an increase of Fe and Ni on the surface of the nanoparticles. Fe and Ni atoms are known to diffuse to the surface of a structure, not into the bulk, and provides a possible mechanism to explain the surface changes. Overall, the chemical surface changes are similar for all of the nanoparticles despite different molar ratios. Batch reactor studies with the azo dye Orange G demonstrated that the removal of Orange G, as measured by UV-visible spectrophotometry, is directly dependent on the composition of the bimetallic nanoparticles. Second order kinetic rate constants for the first 20 min of Orange G removal decrease with increasing Ni to Fe molar ratio, suggesting optimal removal efficiency is achieved at lower Ni:Fe ratios. After the first 20 min of dye removal, the reaction shifts to a zeroth order rate equation, and the rate constant increases with increasing Ni to Fe molar ratio, suggesting that higher nickel content enables longer reactive lifetime. The results of this study demonstrate the need to understand how the composition of NiFe bimetallic nanoparticles impacts contaminant removal kinetics and illustrate an important trade-off between initial reactivity and reactive lifetime.

REFERENCES

[1] E. Forgacs, T. Cserháti, and G. Oros, "Removal of synthetic dyes from wastewaters: A review," *Environ. Int.*, vol. 30, no. 7, pp. 953–971, 2004.

[2] P. A. Carneiro, G. A. Umbuzeiro, D. P. Oliveira, and M. V. B. Zanoni, "Assessment of water contamination caused by a mutagenic textile effluent/dyehouse effluent bearing disperse dyes," *J. Hazardous Mater.*, vol. 174, no. 1–3, pp. 694–699, 2010.

[3] T. Platzek, C. Lang, G. Grohmann, U. S. Gi, and W. Baltes, "Formation of a carcinogenic aromatic amine from an azo dye by human skin bacteria in vitro," (in English), *Hum. Exp. Toxicol.*, vol. 18, no. 9, pp. 552–559, Sep. 1999.

[4] M.-M. Zhang *et al.*, "Comparative study on characteristics of azo dye decolorization by indigenous decolorizers," *Bioresour. Technol.*, vol. 101, no. 8, pp. 2651–2656, 2010.

[5] S. D. Z. Carmen, "Textile organic dyes-characteristics, polluting effects and separation/elimination procedures from industrial effluents-a critical overview," in *Organic Pollutants Ten Years After the Stockholm Convention – Environmental and Analytical Update*. T. Puzyn and A. Mostrag-Szlichtyng ed.: InTech, 2012, ch. 3, pp. 55–86. [Online]. Available: http://dx.doi.org/10.1016/j.arabjc.2016.04.010

[6] J. Fan, Y. Guo, J. Wang, and M. Fan, "Rapid decolorization of azo dye methyl orange in aqueous solution by nanoscale zerovalent iron particles," *J. Hazard. Mater.*, vol. 166, no. 2–3, pp. 904–910, 2009.

[7] X. Liu, Z. Chen, Z. Chen, M. Megharaj, and R. Naidu, "Remediation of direct black G in wastewater using kaolin-supported bimetallic Fe/Ni nanoparticles," *Chem. Eng. J.*, vol. 223, no. 1, pp. 764–771, 2013.

[8] A. D. Bokare, R. C. Chikate, C. V. Rode, and K. M. Paknikar, "Iron-nickel bimetallic nanoparticles for reductive degradation of azo dye orange G in aqueous solution," *Appl. Catal. B: Environ.*, vol. 79, no. 3, pp. 270–278, 2008.

[9] J. Liu, L. Wang, J. Tang, and J. Ma, "Photocatalytic degradation of commercially sourced naphthenic acids by TiO_2-graphene composite nanomaterial," *Chemosphere*, vol. 149, no. 1, pp. 328–335, 2016.

[10] K. Tahir *et al.*, "Visible light photo catalytic inactivation of bacteria and photo degradation of methylene blue with Ag/TiO_2 nanocomposite prepared by a novel method," *J. Photochem. Photobiol. B: Biol.*, vol. 162, no. 1, pp. 189–198, 2016.

[11] E. Saputra, S. Muhammad, H. Sun, H. M. Ang, M. O. Tadé, and S. Wang, "Different crystallographic one-dimensional MnO_2 nanomaterials and their superior performance in catalytic phenol degradation," *Environ. Sci. Technol.*, vol. 47, no. 11, pp. 5882–5887, 2013.

[12] J. Zhang *et al.*, "Synthesis of magnetic iron oxide nanoparticles onto fluorinated carbon fabrics for contaminant removal and oil-water separation," *Sep. Purif. Technol.*, vol. 174, no. 1, pp. 312–319, 2017.

[13] S. Agarwal, I. Tyagi, V. K. Gupta, S. Mashhadi, and M. Ghasemi, "Kinetics and thermodynamics of malachite green dye removal from aqueous phase using iron nanoparticles loaded on ash," *J. Mol. Liquids*, vol. 223, no. 1, pp. 1340–1347, 2016.

[14] Y.-H. Ou, C.-Y. Wei, and Y.-H. Shih, "Short-chain organic acids increase the reactivity of zerovalent iron nanoparticles toward polychlorinated aromatic pollutants," *Chem. Eng. J.*, vol. 284, no. 1, pp. 372–379, 2016.

[15] T. Phenrat and I. Kumloet, "Electromagnetic induction of nanoscale zerovalent iron particles accelerates the degradation of chlorinated dense non-aqueous phase liquid: Proof of concept," *Water Res.*, vol. 107, no. 1, pp. 19–28, 2016.

[16] C. Tan *et al.*, "Radical induced degradation of acetaminophen with Fe_3O_4 magnetic nanoparticles as heterogeneous activator of peroxymonosulfate," *J. Hazard. Mater.*, vol. 276, no. 1, pp. 452–460, 2014.

[17] T. M. Salem Attia, X. L. Hu, and D. Q. Yin, "Synthesized magnetic nanoparticles coated zeolite for the adsorption of pharmaceutical compounds from aqueous solution using batch and column studies," *Chemosphere*, vol. 93, no. 9, pp. 2076–2085, 2013.

[18] T. Liu, X. Yang, Z.-L. Wang, and X. Yan, "Enhanced chitosan beads-supported Fe0-nanoparticles for removal of heavy metals from electroplating wastewater in permeable reactive barriers," *Water Res.*, vol. 47, no. 17, pp. 6691–6700, 2013.

[19] S. Lin, M. Xu, W. Zhang, X. Hua, and K. Lin, "Quantitative effects of amination degree on the magnetic iron oxide nanoparticles (MIONPs) using as adsorbents to remove aqueous heavy metal ions," *J. Hazardous Mater.*, 2017, doi: http://doi.org/10.1016/j.jhazmat.2017.01.016.

[20] J. R. Perey, P. C. Chiu, C. P. Huang, and D. K. Cha, "Zero-valent iron pretreatment for enhancing the biodegradability of azo dyes," (in English), *Water Environ. Res.: A Res. Publication Water Environ. Federation*, vol. 74, no. 3, pp. 221–225, May/Jun. 2002.

[21] F. Fu, Z. Cheng, and J. Lu, "Synthesis and use of bimetals and bimetal oxides in contaminants removal from water: A review," *RSC Adv.*, vol. 5, no. 104, pp. 85395–85409, 2015.

[22] V. K. Vidhu and D. Philip, "Catalytic degradation of organic dyes using biosynthesized silver nanoparticles," *Micron*, vol. 56, no. 1, pp. 54–62, 2014.

[23] M. Ghaedi, S. Heidarpour, S. Nasiri Kokhdan, R. Sahraie, A. Daneshfar, and B. Brazesh, "Comparison of silver and palladium nanoparticles loaded on activated carbon for efficient removal of methylene blue: Kinetic and isotherm study of removal process," *Powder Technol.*, vol. 228, no. 1, pp. 18–25, 2012.

[24] W.-J. Liu, T.-T. Qian, and H. Jiang, "Bimetallic fe nanoparticles: Recent advances in synthesis and application in catalytic elimination of environmental pollutants," *Chem. Eng. J.*, vol. 236, no. 1, pp. 448–463, 2014.

[25] Z. Bao, L. Ye, B. Fang, and L. Zhao, "Synthesis of Fe$_{0.32}$Co$_{0.68}$/γ-Al$_2$O$_3$@C nanocomposite for depth treatment of dye sewage based on adsorption and advanced catalytic oxidation," *J. Mater. Chem. A*, vol. 5, no. 14, pp. 6664–6676, 2017.

[26] H. Sarvari, E. K. Goharshadi, S. Samiee, and N. Ashraf, "Removal of methyl orange from aqueous solutions by ferromagnetic Fe/Ni nanoparticles," *Phys. Chem. Res.*, vol. 6, no. 2, pp. 433–446, 2018.

[27] Y. Lin, Z. Chen, M. Megharaj, and R. Naidu, "Degradation of scarlet 4BS in aqueous solution using bimetallic Fe/Ni nanoparticles," *J. Colloid. Interface Sci.*, vol. 381, no. 1, pp. 30–35, 2012.

[28] R. D. Kale and P. B. Kane, "Colour removal of phthalocyanine based reactive dye by nanoparticles," *Groundwater Sustain. Develop.*, vol. 8, no. 1, pp. 309–318, 2019.

[29] S. L. Foster, K. Estoque, M. Voecks, N. Rentz, and L. F. Greenlee, "Removal of synthetic azo dye using bimetallic nickel-iron nanoparticles," *J. Nanomater.*, vol. 2019, no. 1, pp. 1–12, 2019.

[30] A. D. Bokare, R. C. Chikate, C. V. Rode, and K. M. Paknikar, "Effect of surface chemistry of Fe/Ni nanoparticles on mechanistic pathways of azo dye degradation," *Environ. Sci. Technol.*, vol. 41, no. 21, pp. 7437–7443, 2007.

[31] L. F. Greenlee and S. A. Hooker, "Development of stabilized zero valent iron nanoparticles," *Desalin. Water Treat.*, vol. 37, no. 1–3, pp. 114–121, 2012.

[32] L. F. Greenlee and N. S. Rentz, "ATMP-stabilized iron nanoparticles: Chelator-controlled nanoparticle synthesis," (in English), *J. Nanoparticle Res., Article*, vol. 16, no. 11, Nov. 2014, Art no. 2712.

[33] S. L. Candelaria et al., "Multi-component fe-Ni hydroxide nanocatalyst for oxygen evolution and methanol oxidation reactions under alkaline conditions," *ACS Catal.*, vol. 7, no. 1, pp. 365–379, 2017.

[34] L. F. Greenlee, J. D. Torrey, R. L. Amaro, and M. W. Shaw, "Kinetics of zero valent iron nanoparticle oxidation in oxygenated water," *Environ. Sci. Technol.*, vol. 46, no. 23, pp. 12913–12920, 2012.

[35] S. J. Wilson and L. F. Greenlee, "Morphological and oxidative effects of post-synthesis handling and storage on zero-valent iron nanoparticles," *J. Nanosci. Nanotechnol.*, vol. 17, no. 4, pp. 2413–2422, 2017.

[36] L. F. Greenlee, J. D. Torrey, R. L. Amaro, and J. M. Shaw, "Kinetics of zero valent iron nanoparticle oxidation in oxygenated water," *Environ. Sci. Technol.*, vol. 46, no. 23, pp. 12913–12920, 2012.

[37] Y. Chen, X. Luo, G.-H. Yue, X. Luo, and D.-L. Peng, "Synthesis of iron–nickel nanoparticles via a nonaqueous organometallic route," *Mater. Chem. Phys.*, vol. 113, no. 1, pp. 412–416, 2009.

[38] I. Ban, M. Drofenik, and D. Makovec, "The synthesis of iron–nickel alloy nanoparticles using a reverse micelle technique," *J. Magn. Magn. Mater.*, vol. 307, no. 2, pp. 250–256, 2006.

[39] K. S. Dijith, R. Aiswarya, M. Praveen, S. Pillai, and K. P. Surendran, "Polyol derived Ni and nife alloys for effective shielding of electromagnetic interference," *Mater. Chem. Front.*, vol. 2, no. 10, pp. 1829–1841, 2018.

[40] S. Hosseynizadeh Khezri, A. Yazdani, and R. Khordad, "Pure iron nanoparticles prepared by electric arc discharge method in ethylene glycol," *Eur. Phys. J. Appl. Phys.*, vol. 59, no. 3, 2012.

[41] N. Ezzatahmadi et al., "Catalytic degradation of orange II in aqueous solution using diatomite-supported bimetallic Fe/Ni nanoparticles," *RSC Adv.*, vol. 8, no. 14, pp. 7687–7696, 2018.

[42] S. Ravi and A. Kartikeyan, "Magnetically tunable superparamagnetic cobalt doped iron oxide colloidal nanocluster," *Adv. Mater. Lett.*, vol. 4, no. 7, pp. 562–566, 2013.

[43] M. K. Ghosh, G. E. J. Poinern, T. B. Issa, and P. Singh, "Arsenic adsorption on goethite nanoparticles produced through hydrazine sulfate assisted synthesis method," *Korean J. Chem. Eng.*, vol. 29, no. 1, pp. 95–102, 2011.

[44] P. Acharya et al., "Chemical structure of fe-Ni nanoparticles for efficient oxygen evolution reaction electrocatalysis," *ACS Omega*, vol. 4, no. 17, pp. 17209–17222, Oct. 2019.

[45] N. S. McIntyre and D. G. Zetaruk, "X-ray photoelectron spectroscopic studies of iron oxides," *Anal. Chem.*, vol. 49, no. 11, 1977.

[46] A. P. Grosvenor, B. A. Kobe, M. C. Biesinger, and N. S. McIntyre, "Investigation of multiplet splitting of Fe 2p XPS spectra and bonding in iron compounds," *Surf. Interface Anal.*, vol. 36, no. 12, pp. 1564–1574, 2004.

[47] W. Temesghen and P. M. Sherwood, "Analytical utility of valence band X-ray photoelectron spectroscopy of iron and its oxides, with spectral interpretation by cluster and band structure calculations," *Anal. Bioanal. Chem.*, vol. 373, no. 7, pp. 601–608, Aug. 2002.

[48] T. Yamashita and P. Hayes, "Analysis of XPS spectra of Fe^{2+} and Fe^{3+} ions in oxide materials," *Appl. Surf. Sci.*, vol. 254, pp. 2441–2449, 2008.

[49] V. M. Dhavale, S. K. Singh, A. Nadeema, S. S. Gaikwad, and S. Kurungot, "Nanocrystalline Fe-Fe$_2$O$_3$ particle-deposited N-doped graphene as an activity-modulated Pt-free electrocatalyst for oxygen reduction reaction," *Nanoscale*, vol. 7, no. 47, pp. 20117–20125, 2015.

[50] M. Lasserus, D. Knez, M. Schnedlitz, A. W. Hauser, F. Hofer, and W. E. Ernst, "On the passivation of iron particles at the nanoscale," *Nanoscale Adv.*, vol. 1, no. 6, pp. 2276–2283, 2019.

[51] Z. Wu, X. L. Huang, Z. L. Wang, J. J. Xu, H. G. Wang, and X. B. Zhang, "Electrostatic induced stretch growth of homogeneous beta-Ni(OH)2 on graphene with enhanced high-rate cycling for supercapacitors," *Sci. Rep.*, vol. 4, no. 1, 2014, Art. no. 3669.

[52] C. Ding et al., "A bubble-template approach for assembling ni-co oxide hollow microspheres with an enhanced electrochemical performance as an anode for lithium ion batteries," *Phys. Chem. Chem. Phys. : PCCP*, vol. 18, no. 37, pp. 25879–25886, 2016.

[53] P. Acharya and L. F. Greenlee, "Iron-Nickel alloy mixed oxide shell nanoparticles," *Pat. Utility Pat. Filed*, May 2018.

[54] X. Shen et al., "Oxidation-Induced atom diffusion surf. Restructuring faceted ternary Pt–Cu–Ni nanoparticles," *Chem. Mater.*, vol. 31, no. 5, pp. 1720–1728, 2019.

[55] Y. Ge et al., "Highly mesoporous hierarchical nickel and cobalt double hydroxide composite: Fabrication, characterization and ultrafast NO$_x$ gas sensors at room temperature," *J. Mater. Chem. A*, vol. 2, no. 14, 2014.

[56] X. Rong, F. Qiu, J. Qin, H. Zhao, J. Yan, and D. Yang, "A facile hydrothermal synthesis, adsorption kinetics and isotherms to congo red azo-dye from aqueous solution of Nio/graphene nanosheets adsorbent," *J. Ind. Eng. Chem.*, vol. 26, no. 1, pp. 354–363, 2015.

[57] H. Ali-Löytty et al., "Ambient-pressure XPS study of a Ni–Fe electrocatalyst for the oxygen evolution reaction," *J. Phys. Chem. C*, vol. 120, no. 4, pp. 2247–2253, 2016.

[58] N. Weidler et al., "X-ray photoelectron spectroscopic investigation plasma-enhanced chemical vapor deposited NiO$_x$, NiO$_x$(OH)$_y$, and CoNiO$_x$(OH)$_y$: Influence of the chemical composition on the catalytic activity for the oxygen evolution reaction," *J. Phys. Chem. C*, vol. 121, no. 12, pp. 6455–6463, 2017.

[59] F. He and D. Y. Zhao, "Manipulating the size and dispersibility of zerovalent iron nanoparticles by use of carboxymethyl cellulose stabilizers," (in English), *Environ. Sci. Technol., Article*, vol. 41, no. 17, pp. 6216–6221, 2007.

[60] I. A. Ike et al., "Advanced oxidation of orange G using phosphonic acid stabilised zerovalent iron," *J. Environ. Chem. Eng.*, vol. 5, no. 4, pp. 4014–4023, 2017.